remote sensing

MDPI

Article

Performance Evaluation and Noise Mitigation of the FY-3E Microwave Humidity Sounder

Jiali Mao [1,2], Zhengkun Qin [1,2,*], Juan Li [3,4], Yang Han [3,4] and Jing Huang [3,4]

[1] Collaborative Innovation Center on Forecast and Evaluation of Meteorological Disasters, Nanjing University of Information Science and Technology, Nanjing 211544, China
[2] Joint Center for Data Assimilation for Research and Application, Nanjing University of Information Science and Technology, Nanjing 211544, China
[3] CMA Earth System Modeling and Prediction Centre, Beijing 100081, China
[4] State Key Laboratory of Severe Weather, Beijing 100081, China
* Correspondence: qzk_0@nuist.edu.cn

Abstract: Fengyun-3E, which is equipped with MicroWave Humidity Sounder 2 (MWHS-2) for detecting both temperature and humidity, is China's latest polar orbiting meteorological satellite and China's first satellite in early-morning orbit. The observation bias and observation error characteristics of MWHS-2 are evaluated by using ERA-5 as the background field. The results show that the biases range from −4 to 2 K, and the observation errors are within 1.5 K except for the window channels. A further analysis of the dependence on the scanning angles indicates that observation errors for the window channels and the 118-GHz channels increase with decreasing scanning angles. Observation errors of the window channels and water vapor channels are also latitudinally dependent, and the maximum errors in the high latitudes reach 2.0 K, while those in the tropical regions are approximately 0.8 K. In addition, the observed brightness temperature of FY-3E MWHS-2 is accompanied by striping noises along the track and high-frequency oscillation noises along the scanlines. The noise mitigation results show that both noises are approximately 0.2 K.

Keywords: Fengyun-3E; MWHS-2; data evaluation; noise mitigation

Citation: Mao, J.; Qin, Z.; Li, J.; Han, Y.; Huang, J. Performance Evaluation and Noise Mitigation of the FY-3E Microwave Humidity Sounder. *Remote Sens.* **2022**, *14*, 4835. https://doi.org/10.3390/rs14194835

Academic Editors: Dongryeol Ryu and Zhenzhan Wang

Received: 18 July 2022
Accepted: 23 September 2022
Published: 28 September 2022

1. Introduction

Fengyun-3E (FY-3E), which is China's first early-morning orbit satellite, was successfully launched from Jiuquan Satellite Launch Center in Gansu Province on 5 July 2021. This satellite is the fifth satellite in the Fengyun-3 series, which was designed for meteorological operations, marine monitoring, climate monitoring, atmospheric chemistry and space weather. FY-3E crosses the equator (descending node) between 5:30 and 5:50 local solar time, which fills in the gap of satellite observations within the 6-h assimilation window and provides atmospheric state profiles every 4 h to the global data assimilation system. FY-3E adopts a three-axis stabilized system with an orbital altitude of 836 km and an inclination of 98.75°. The orbital period and the quasi-repeat time are 101.5 min and 5.5 days, respectively [1].

FY-3E is equipped with 11 devices, including the Microwave Humidity Sounder 2 (MWHS-2), which is able to detect the atmosphere under all weather conditions (except for precipitation) and provide global coverage of atmospheric temperature and humidity profiles. Therefore, MWHS-2 will play a key role in numerical weather predictions (NWPs), data assimilation and weather/climate monitoring [2–5].

Satellite data assimilation is a crucial step that improves NWPs. The data assimilation method uses the observations provided by satellites to adjust the background field, with the assumption that both the observation data and the background field have only unbiased Gaussian errors [6]. To obtain the initial field of the NWP model that is closest to the truth, the differences between the observed and simulated brightness temperatures ("O−B") and

the unbiased errors of each are integrated to adjust the background field [7]). The error characteristics of the observation data are important references for data assimilation, before which the error estimation and bias correction must be performed on the observations.

Moreover, data assimilation is largely influenced by the error and bias characteristics of satellite observations [8,9]. Observation error (mainly including instrument observation error and data representative error) is generally used to determine the weights of the observation data in assimilation [10] and is an important factor in determining whether the observations can be effectively used and whether the analysis field can provide optimal estimation of the atmospheric state [11]. Many studies have focused on the characteristics of observation errors in specific situations [12,13]. Qin and Zou [14] improved microwave data assimilation in plateau regions by adjusting the observation errors of different vegetation types. Qin [15] also found that Landsat data utilization can be significantly improved by clarifying the error characteristics of each channel.

Additionally, an effective bias correction scheme is very important to ensure unbiased observation error [16]. Zhao et al. [17] improved the soil moisture simulation in the Community Land Model Version 4 by assimilating the brightness temperature observed by the Advanced Microwave Scanning Radiometer for EOS (AMSR-E) and emphasized the effect of bias correction on the AMSR-E brightness temperature. Li et al. [18] proposed a bias correction scheme for the Cross-Track Infrared Sounder assimilation by considering the bias dependence on the latitude and scanning angles, which proved that this method has better performance than the traditional air mass bias correction scheme in the regional NWP model. In addition, many studies have focused on adaptive bias correction methods [6,19]. Han et al. [20] developed a constrained variational bias correction scheme by adding a new constraint term to the variational cost function. This new method successfully constrains the drift during bias correction and provides a more stable assimilation system for long-term reanalysis data construction.

The evaluation of instrument errors and biases has been given much attention by many researchers because of its great effect on data assimilation. The observation data of each instrument require meticulous error analysis before assimilation application. Lu et al. [21] conducted a detailed evaluation of the Fengyun-3A microwave temperature sounder (MWTS) and found obvious frequency drift; Guan et al. [22] compared the MicroWave Humidity Sounder 1 (MWHS-1) carried by Fengyun-3A with the Microwave Humidity Sounding carried by NOAA-18 and found that the two instruments have similar error characteristics in the upper-level sounding channels; Wang and Zou [23] discovered that the observations of the Fengyun-3B MWTS-1 Channel 4 are contaminated in a small latitude band ($-30°$N$\sim 40°$N) in the Northern Hemisphere; Han and Hou [24] found that the brightness temperature simulated by the Community Radiative Transfer Model and Radiative Transfer for TIROS Operational Vertical Sounder (RTTOV) are different for FY-3D MWTS-2 Channels 4 and 11 and that the long-term bias weakly depends on latitude.

As China's first early-morning orbit satellite, the observation times of FY-3E are different from those of the existing polar orbiting satellites. Therefore, clarifying the bias and error characteristics of its observations before data assimilation is particularly important. In this paper, the European Centre for Medium-Range Weather Forecasting (ECMWF) Fifth-Generation Reanalysis (ERA-5) is used as the background field [25], and RTTOV is selected as the radiative transfer model (RTM) to estimate the bias and error characteristics of FY-3E MWHS-2 over the Pacific Ocean under clear-sky conditions from September to October.

The article is organized as follows. the channel characteristics of MWHS-2 are shown in Section 2. The brightness temperature in instrumental observations and model simulations are described in Section 3; the introduction to the RTM and its input variables are also included in this section. The biases and standard deviations of the "O−B", including their dependences on scanning angles and latitudes, are discussed in detail in Section 4. A brief introduction to the method that is used for separating observation noises and showing the extracted striping noises and along-scan noises is provided in Section 5. The

improvement of the "O−B" after noise mitigation is also discussed in Section 5. A summary and conclusions are given in Section 6.

2. Introduction to the Instruments

FY-3E MWHS-2 has 98 fields of view (FOVs), with a horizontal spatial resolution of 16 km at nadir points and a swath width of 2700 km. The instrument adopts the cross-track scanning mode. The Earth sense scanning angle is between $\pm 53.35^\circ \pm 0.1^\circ$ with a scan cycle of 8/3 s. The antenna pointing accuracy is $\pm 0.8^\circ$, and the nadir pointing error is less than 0.2°. The instrument adopts 360° variable-speed scanning by default. Moreover, uniform scanning and fixed-angle observation according to command are also achievable. The periodic two-point calibration method is still adopted for on-orbit calibration. The parameters of the 15 channels are listed in Table 1. Channels 1 and 10 are the two window channels for monitoring background microwave radiation and precipitation. Channels 2 to 9, situated near the oxygen absorption line of 118.75 GHz (hereafter referred to as the 118-GHz channel for simplicity), are the unique channels for MWHS-2. In contrast to the oxygen absorption line near 60 GHz, the 118-GHz oxygen absorption line is more sensitive to clouds and precipitation and can be used for vertical temperature detection as well as the retrieval of cloud and precipitation parameters [26]. Channels 11 to 15 centered on the water vapor absorption line at 183.31 GHz are designed to obtain the distributions of atmospheric humidity at different layers of the troposphere. Both the 118-GHz channels and water vapor absorption channels are set as double-sideband channels to improve detection sensitivity [27]. Although inheriting the technical system of the Batch 2 Type II microwave humidity sounders, FY-3E MWHS-2 is different from the humidity sounder, also named MWHS-2, that is carried by FY-3C/3D in channel setting, sensitivity and calibration accuracy. Specifically, the frequency is changed from 150 GHz to 166 GHz for Window Channel 10; except for Channel 2, the other channels have a nearly twofold increase in sensitivity, and the calibration accuracy (the expectation for sensitivity after calibration in instrument design, representing the minimum temperature difference that can be resolved by the instrument) is improved as well [1]. More technical details of the instrument can be found on the website of Fengyun meteorological satellite [28].

Table 1. Channel number, central frequency (unit: GHz), polarization (QV and QH represent quasi-vertical and quasi-horizontal polarization, respectively), bandwidth (unit: MHz), noise equivalent differential temperature (NEΔT, unit: K) and calibration accuracy (unit: K) of MWHS-2.

Channel Number	Central Frequency	Polarization	Bandwidth	NEΔT	Calibration Accuracy
1	89.0	QH	1500	0.4	1.0
2	118.75 ± 0.08	QV	20	2.2	2.4
3	118.75 ± 0.2	QV	100	1.0	1.2
4	118.75 ± 0.3	QV	165	0.8	1.2
5	118.75 ± 0.8	QV	200	0.8	1.2
6	118.75 ± 1.1	QV	200	0.8	1.0
7	118.75 ± 2.5	QV	200	0.8	1.0
8	118.75 ± 3.0	QV	1000	0.5	1.0
9	118.75 ± 5.0	QV	2000	0.5	1.0
10	166.0	QH	1500	0.4	1.0
11	183.31 ± 1	QV	500	0.6	1.0
12	183.31 ± 1.8	QV	700	0.6	1.0
13	183.31 ± 3	QV	1000	0.5	1.0
14	183.31 ± 4.5	QV	2000	0.5	1.0
15	183.31 ± 7	QV	2000	0.5	1.0

3. RTM Simulation

Assuming that the background field is an unbiased reference, the calculation of the "O−B" is widely used to estimate the biases and errors of the postlaunch instruments [6].

The vertical profiles of the 15 channels of FY-3E MWHS-2 are shown in Figure 1. The 118-GHz channels (shown as dotted lines) have a wide vertical detection range, which extends from near the surface to approximately 20 hPa, allowing for a complete temperature profile of the atmosphere. The sounding levels of the water vapor absorption channels are evenly distributed vertically, with weighting functions peaking in the range of 900 hPa to 400 hPa. Therefore, this instrument can provide a detailed distribution of humidity in the middle and lower troposphere. As the channel numbering order increased, the sounding level heights of the 118-GHz channels and water vapor absorption channels all decreased.

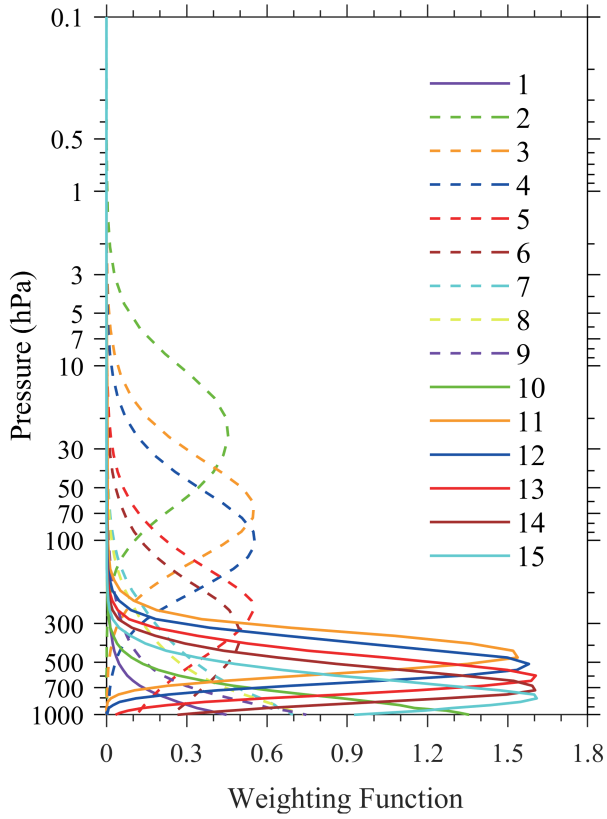

Figure 1. Weighting functions (WFs) for the 15 channels of the MWHS-2 onboard the FY-3E.

Fifteen days of FY-3E MWHS-2 observation data covering the period from 24 September to 8 October 2021, were employed to calculate the bias and errors. In this study, RTTOV Version 13 and ERA-5 data sets with 6-h intervals (UTC 00, 06, 12, 18) were adopted as the RTM and the background field for simulation, respectively.

RTTOV is a fast one-dimensional RTM that allows rapid simulation of radiances for satellite visible, infrared or microwave scanning radiometers given atmospheric temperature profiles, variable gas concentrations, cloud and surface characteristics [29]. The RTTOV has been used extensively to evaluate satellite instruments [30,31] since it was originally developed by the ECMWF in the 1990s to achieve direct assimilation of radiances in its variational system [32]. The ERA-5 data sets used in the clear-sky simulation in this study have a horizontal resolution of 0.25° × 0.25°, with 37 layers in the vertical direction. The top level in the ECMWF analysis model is at 1 hPa. The input variables of the RTTOV include latitude and longitude information, atmospheric state profiles, surface parameters and instrument scanning parameters. The atmospheric state profiles consist of the vertical profiles of pressure, temperature and specific humidity. The surface parameters are listed as follows: (I) surface type, height, temperature and air pressure; (II) sea surface salinity; (III) 2-m temperature, humidity and air pressure; and (IV) 10-m wind speed and direction. The scanning parameters include the zenith and azimuth angles of the satellite and the sun, respectively.

To rule out the uncertainty of the RTM on the cloud simulation and surface emissivity, clear pixels over the Pacific Ocean between 50°S and 50°N are considered to calculate the biases and standard deviations of the "O−B", whose dependence on the scanning angles and latitude bands will also be analyzed later. The criteria for judging clear sky pixels are as follows: (I) the total cloud liquid water path is less than 0.02 kg·m^{-2}; (II) the absolute value of the "O−B" for any channel is less than or equal to 5 K.

Channel 3 and Channel 12 are one of the 118-GHz channels and water vapor absorption channels, with weighting functions peaking at 70 hPa and 500 hPa, respectively. Figure 2 shows the global distributions of the observed brightness temperature (Figure 2a), the model simulated brightness temperature (Figure 2b) and the "O−B" (Figure 2c) (only the ascending orbit) of MWHS-2 Channel 3 on 2 October 2021.

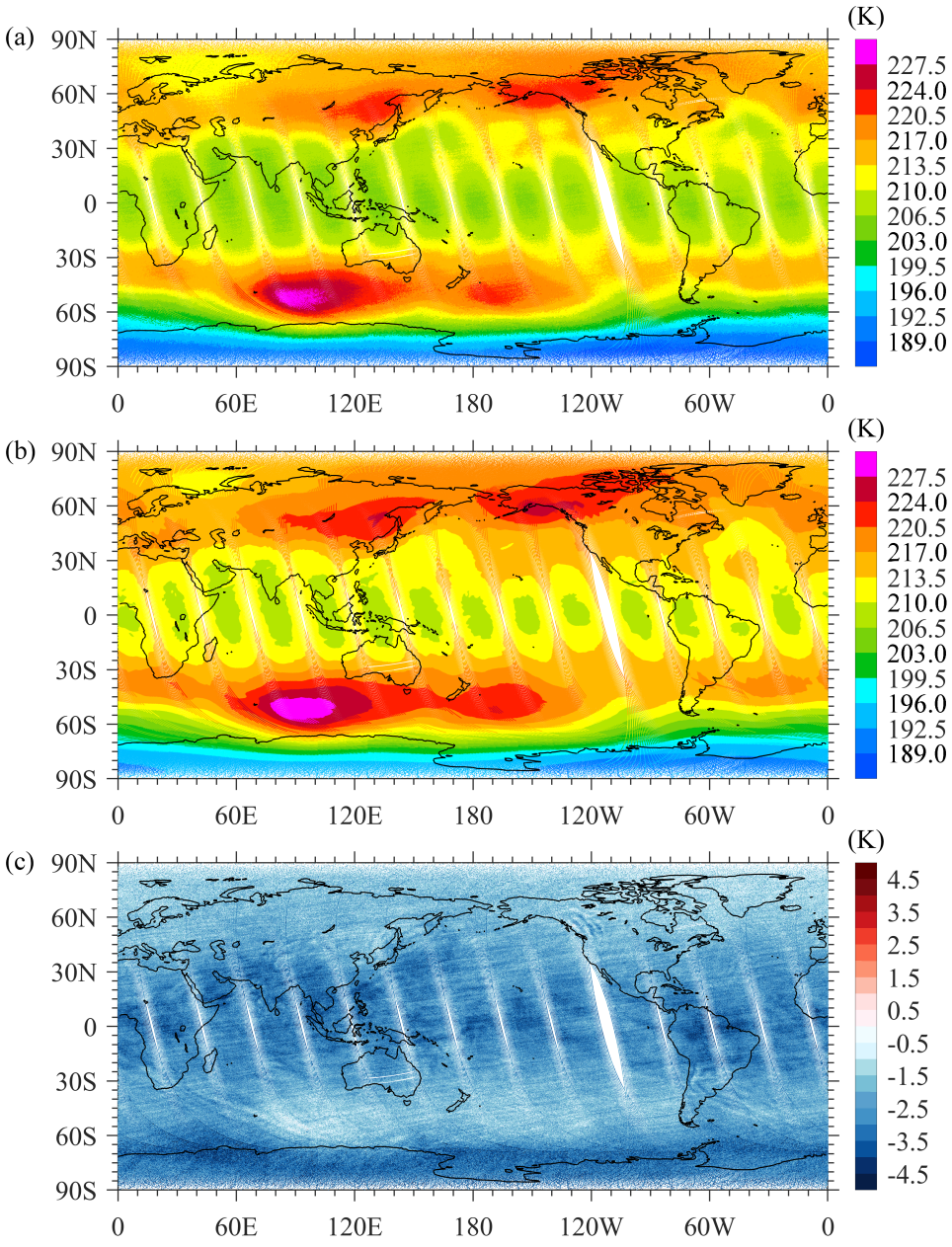

Figure 2. Spatial distribution of the: (**a**) observed; (**b**) simulated brightness temperature (unit: K); and (**c**) the difference (unit: K) between them ("O−B") for MWHS-2 Channel 3 (WF peaks at 70 hPa) on 2 October 2021.

The observed brightness temperature mainly represents the temperature characteristics of the stratosphere, where the temperature in the tropics is lower than that in the middle and high latitudes due to the ozone distribution. The sun shines more directly on the Northern Hemisphere in summer, and the whole North Pole is in the high temperature region. In the Southern Hemisphere, the middle latitudes are characterized by high temperatures, while the Antarctic is characterized by low temperatures. Due to cross-track scanning, the brightness temperature cannot properly reveal the delicate temperature structure in the tropical region, only showing a decrease in the temperature on both sides of the scanlines. Simulations of the brightness temperature reproduce the spatial characteristics of the observation, including the high temperature zones located at the middle and high latitudes in the Northern Hemisphere and the middle latitudes in the Southern Hemisphere as well as the low temperature zone at the South Pole. The RTM also exhibits the limb darkening effect of the Earth sense in the tropical region. However, the brightness temperature simulated by the model is approximately 3.5 K higher than that observed, making the "O−B" distribution uniformly negative. Figure 2c shows that there are obvious striping noises along the tracks in the "O−B" distribution, which will be further discussed in Section 4.

Similar to Figure 2, Figure 3 shows the observation, simulation and "O−B" distribution for Channel 12, which is a water vapor absorption channel whose weighting function peaks at approximately 500 hPa. As displayed in Figure 3a, water vapor in the tropics is obviously higher than that in the middle and high latitudes at 500 hPa, especially in the tropical Southern Hemisphere, where there are several high bright temperature centers. In the Pacific Ocean, the high brightness temperature region is closer to the tropics at approximately 5°S, while that in the Indian Ocean and Atlantic Ocean is close to 20°S. Due to the intense variation in water vapor in the middle troposphere, cross-track scanning has relatively little impact on obtaining the spatial structures of the brightness temperature distribution, reproducing almost all the global extreme centers. Figure 3c shows that the "O−B" in the marine area within 50°S/N mostly exhibits a positive bias. Although the observed and simulated brightness temperature distributions are very similar to each other, many details in the weather systems are not well reproduced in the "O−B" distribution. There are obvious local variations, especially at the edges of the extreme centers where the distribution of the positive and negative values alternates, indicating that there may be a shift in the position of the weather system. The high-latitude region is dominated by negative biases, which may be due to an excessively high surface emissivity setting in snow and ice areas and therefore an overestimation of the background field brightness temperature. In contrast, the absolute values of the "O−B" within 50° S/N are significantly smaller than those at high latitudes. In order to avoid the interference of land surface emissivity error and insufficient accuracy of sea ice information in the background, in the subsequent study, we only selected the data over the ocean. In addition, considering that the Pacific region can provide enough observation data for the study, and also to avoid the impact of including more data along the coastline, this study only focuses on the Pacific region within 50°S/N for the evaluation research.

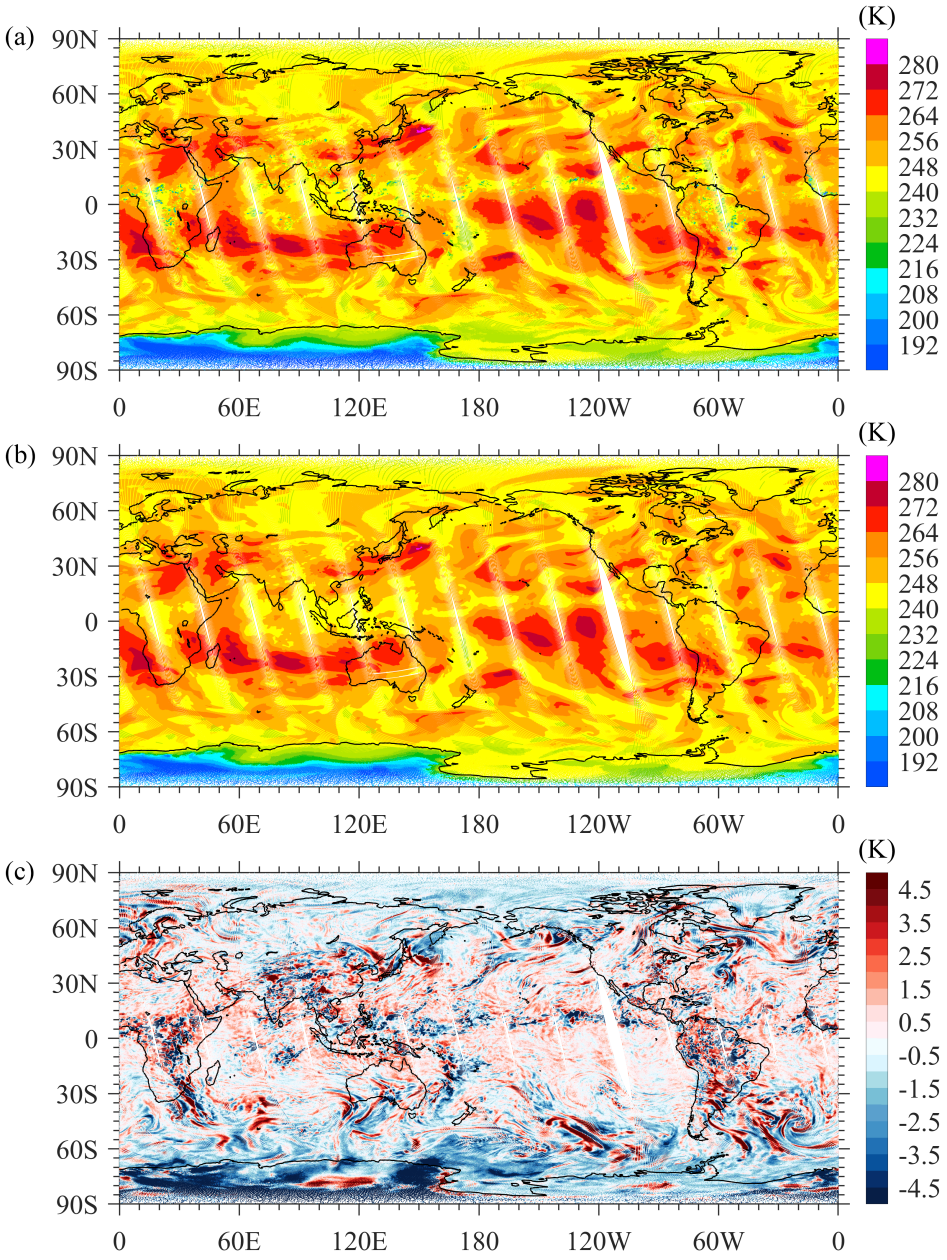

Figure 3. Spatial distribution of the: (**a**) observed; (**b**) simulated brightness temperature (unit: K); and (**c**) the difference (unit: K) between them ("O−B") for Channel 12 (WF peaks at 500 hPa) on 2 October 2021.

4. Bias Characteristics

The "O−B" is assumed to be unbiased in satellite data assimilation and is widely employed to analyze the error characteristics of the instrument. To exclude the influence of clouds and surface emissivity, only clear-sky pixels on the Pacific Ocean were taken as the samples. Figure 4 shows the spatial distributions of clear-sky marine data counts within $2^\circ \times 2^\circ$ grid boxes in the 15-day sampling period on the Pacific Ocean. Most of the regions have more than 400 clear-sky FOVs, except for the regions with less than 100 clear-sky FOVs on the equatorial sides of the eastern Pacific. The area with the highest clear-sky data counts is off Northeast Australia, where the maximum is over 3300, while the areas with less clear-sky FOVs are roughly distributed in the Intertropical Convergence Zone (ITCZ), south of the equator in the eastern Pacific Ocean, northeast of Hawaii, and near the Solomon Islands.

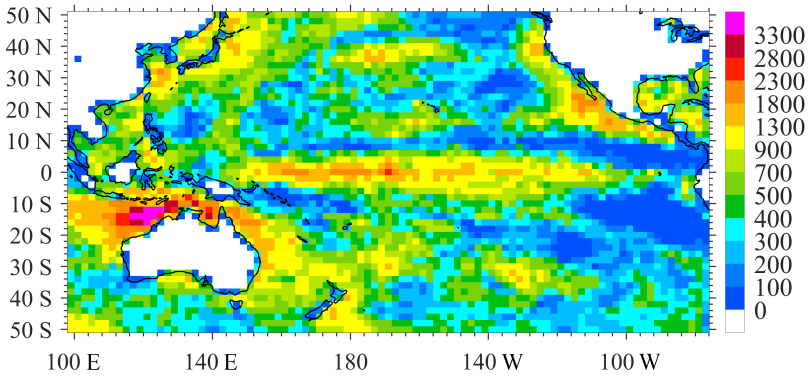

Figure 4. Spatial distributions (color shading) of MWHS-2 clear-sky marine data counts in 2° × 2° grid boxes from 24 September to 8 October 2021.

Using the clear-sky marine data mentioned above, the 15-day mean values and standard deviations of the "O−B" were calculated in this study (see Figure 5). The blue bars and the red dotted line in Figure 5 represent the mean values and the standard deviations of each channel. As displayed by Figure 5a, the bias of each channel is basically between −4 K and 2 K. Moreover, most channels show negative biases except for those in Channel 1, Channel 9 and Channels 11 to 12. The biases of the 118-GHz channels increase with decreasing sounding level heights. For the upper-air sounding Channel 2, the peak weighting function is located at approximately 70 hPa with a bias of −3 K, while Channel 9, whose detection level is close to the ground, is biased by 0.6 K. In contrast, the biases of the water vapor absorption channels decrease from 0.4 K (Channel 11) to −1 K (Channel 15) with decreasing detection heights. The standard deviations of the 15 channels are all less than 2 K, among which those of the two window channels are larger than the others. Channel 1 has the largest standard deviation of approximately 1.9 K, followed by Channel 10 which has 1.75 K. The standard deviations of the 118-GHz channels decrease first, from 1.2 K (Channel 2) to 0.5 K (Channel 6) and then increase with decreasing detection heights to 1.2 K for Channel 9. In contrast, the water vapor absorption channels have continuously deceasing standard deviations from 1.3 K (Channel 11) to 0.9 K (Channel 15). On average, the standard deviations of the water vapor absorption channels are slightly higher than those of the 118-GHz channels.

To test the influence of background field on bias and observation error estimates, the same period of the Final (FNL) Operational Global Analysis data of the National Centers for Environmental Prediction (NCEP) was also used, and the results are shown in Figure 5b. The two evaluation results are very similar except for some slight differences. The bias calculated based on the NCEP FNL data were slightly larger than those of the ERA5 data for Channels 3–8 and Channels 10–12. Moreover, the standard deviations of "O−B" of water vapor absorption channels were slightly larger when using the NCEP FNL as the background field. In general, it can be considered that the influence of the background field on the bias and observation error estimation was very small and can be ignored.

FY3E MWHS-2 is a cross-track detector whose optical path and FOVs change with scanning angles during detection, which will inevitably lead to changes in the biases of the observations. The scan bias of the "O−B" for each channel with FOVs (or scanning angles) is shown in Figure 6. The biases and standard deviations of the 118-GHz channels (left column) and water vapor channels (right column) are presented here for distinction.

For the two window channels, the biases of Channel 1 are positive and vary little with the FOVs, ranging from 1.2 K to 1.6 K. However, the biases of Channel 10 significantly change with the scanning angles, which increased from approximately −1.3 K for the first FOV to approximately 0.4 K for the central FOV and then decreased to approximately −2.4 K for the last FOV. In the 118-Ghz channel, the deviation of Channel 2 hardly changes with the field of view. The absolute values of the biases of Channels 3 and 4 at both ends of the scanlines are approximately 0.4 K smaller than those in the middle. For Channels 5 to 9,

the absolute bias values generally increase with increasing scanning angles (except for the FOVs near the endpoint). The maximum bias difference between Channels 5 and 6 is approximately 0.4 K, and that between Channels 7 and 9 is approximately 1.3 K, which may result from the vertical gradient of temperature. For all the water vapor absorption channels, the average bias of the first 49 FOVs is slightly larger than that of the last 49 FOVs, which may be due to the polarization misalignment in the radiometer receiver [33]. Figure 6a,b show a jagged change in the bias along the scanning direction, which is recognized as the high-frequency oscillating noise related to the scanning positions and will be further discussed in Section 4. The same calculation is performed using the NCEP FNL data as the background field. It can be seen from Figure 7 that the high-frequency oscillating noises still exist in the biases of each channel, indicating that the noise exists in the instrument observation and is independent of the background field.

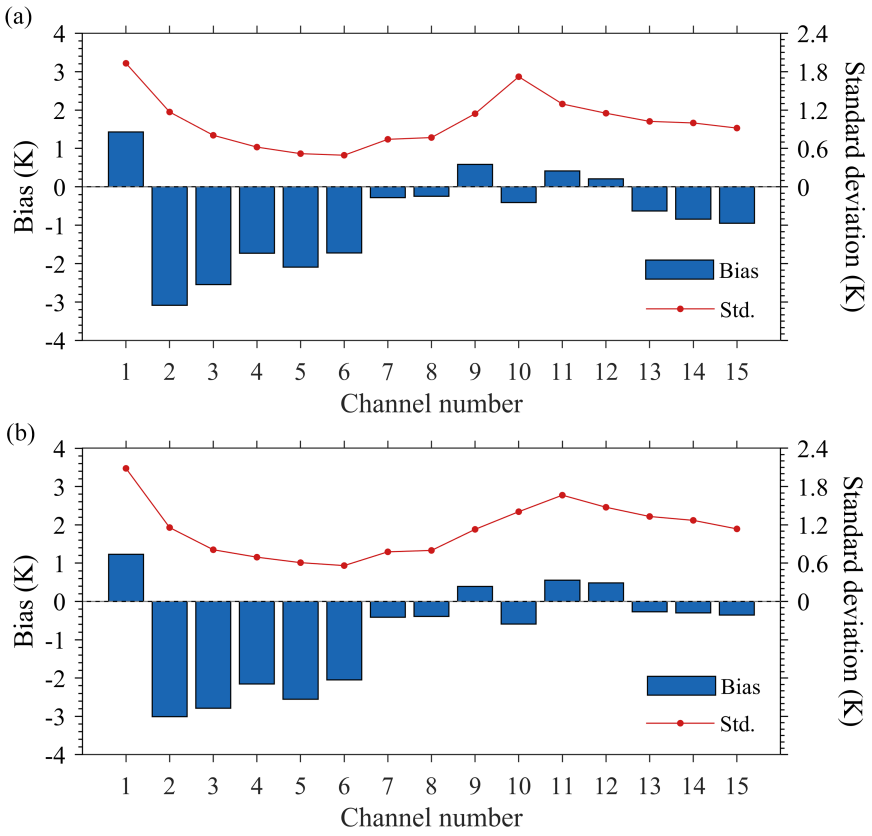

Figure 5. Biases (blue bars, unit: K) and standard deviations (red dotted curves, unit: K) of the "O−B" calculated from clear-sky marine pixels based on the background field of: (**a**) ERA-5; and (**b**) NCEP FNL, respectively. The calculation covers the period from 24 September to 8 October 2021.

According to Figure 6c,d, the standard deviations for the window channels (i.e., Channel 1 and Channel 10) and the 118-GHz channels are basically symmetrical with respect to the magnitude of scanning angles. The standard deviations in the 12 FOVs at both ends of the scanlines for the two window channels significantly decrease with increasing scanning angles. The decreasing gradient of Channel 1 is approximately 0.03 K/FOV and that of Channel 10 is approximately 0.06 K/FOV, while the standard deviations in the central 74 FOVs show no dependence on the scanning angles. Among the 118-GHz channels, the standard deviations of Channels 7 to 9 gradually decrease from the center to the two ends of the scanline, with decreases of approximately 0.2 K (Channel 7), 0.3 K (Channel 8), and 0.5 K (Channel 9), respectively. The other 118-GHz and water vapor absorption channels do not appear to have a scanning angle dependence in their standard deviations.

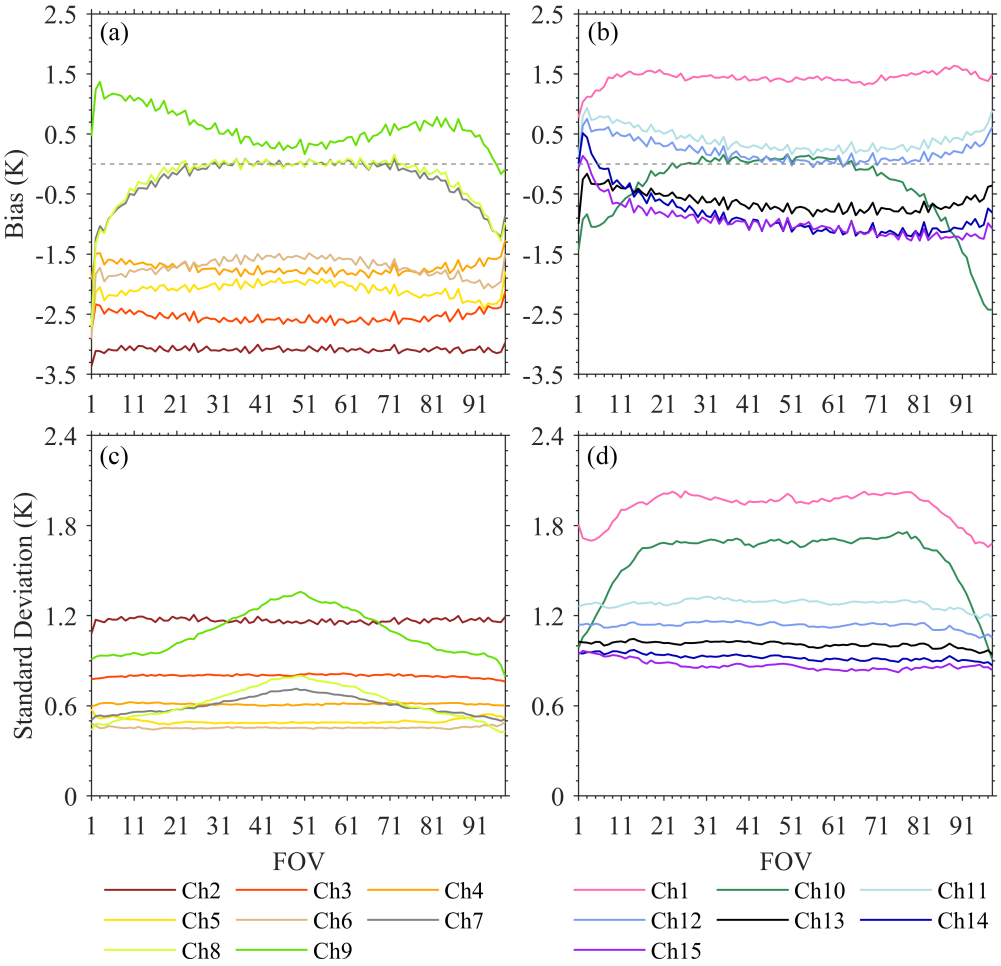

Figure 6. Variations of the biases ((**a**,**b**), unit: K) and standard deviations ((**c**,**d**), unit: K) with the 98 FOVs for the 15 channels. The left column indicates the results of the 118-GHz channels, and the right column indicates the other channels.

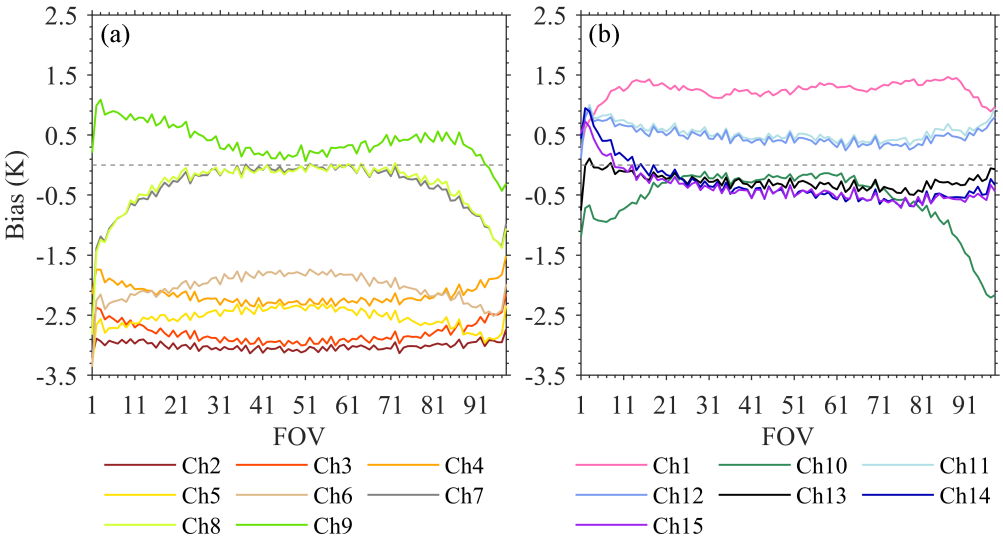

Figure 7. Variations of the biases for (**a**) the 118-GHz channels and (**b**) the other channels with FOVs using the NCEP FNL data as the background field.

Figure 8a,b show latitudinal dependencies of the biases and standard deviations of the "O−B" brightness temperature for 15 channels. The most obvious negative bias is in Channels 2 near 118.75 GHz, whose magnitude reaches a maximum of approximately 3.6 K in the latitudinal bands of −15°S to 15°N. In contrast, the bias absolute values of the low-level sounding channels are smaller, basically within ±1.0 K. Notably, except for the window channels, all the other channels show a certain latitude dependence. For the 118-GHz channels, the absolute biases in the high-latitude zones are obviously smaller than those in the tropical regions, and for the water vapor absorption channels, biases (including the sign) decrease with the increasing latitude. Moreover, the standard deviations for the water vapor absorption channels are more latitudinally dependent compared to the 118-GHz channels, with large values appearing at near 50° S/N and decreasing toward the tropics. In addition, the observation errors continuously increase with the detection heights, corresponding to the distribution characteristics of atmospheric water vapor. In comparison, the standard deviations of the 118-GHz channels are relatively stable, but the observation errors also increase with decreasing latitude, indicating that the data assimilation needs a bias correction scheme and adjustment to the observation weight according to the latitudinal characteristics.

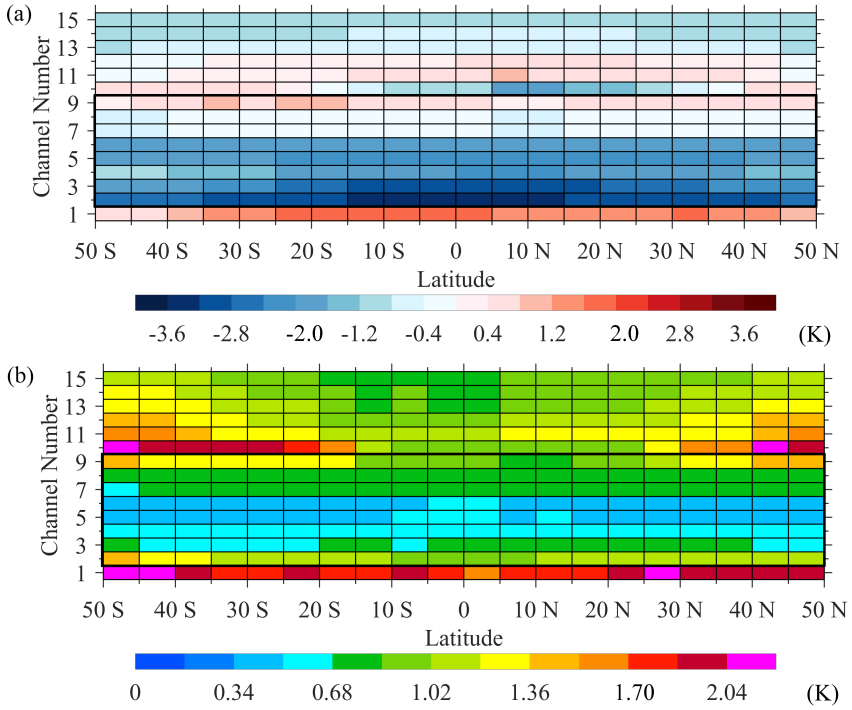

Figure 8. Latitudinal dependence values of the: (**a**) biases (unit: K); and (**b**) standard deviations (unit: K) of the "O−B" calculated in each 5° latitudinal band between 50° S and 50° N. The black box represents the 118-GHz channels.

In order to prove the suitability of the background field, ERA-5, the spatial distribution of the "O−B" standard deviation for Channels 6 and 13 are presented, as well as the spatial distribution of the variability of ERA-5's atmospheric temperature and specific humidity at the heights where the peak weighting functions of the two channels located. To calculate the standard deviation and variability, we first convert the data to grid data. The mesh division is consistent with Figure 4 in the paper. Standard deviations are calculated based on the clear-sky marine pixels located in each 2° × 2° grid box within 15 days. Here, the results of Channels 6 and 13 are displayed to represent the 118-GHz channel and the water vapor absorption channel, respectively.

As can be seen from Figure 9, the standard deviation of "O−B" for Channel 13 is within 2.0 K, and the large values are mainly located in the Sea of Japan, the ocean south

of Australia, and the northeast Pacific. The standard deviation of "O−B" increases significantly with the increasing latitude. Although the large atmospheric temperature variability at 600 hPa also appears in the high latitudes, the comparison between Figures 1b and 9a shows that the standard deviation of "O−B" has little relationship with atmospheric temperature variability since there is no large temperature variability center in the Sea of Japan and the ocean south of Australia and the location of the large value center of temperature variability in the northeast Pacific is significantly different from that of the "O−B" standard deviation. Figure 9c shows the spatial distribution of the variability of specific humidity at 600 hPa. The large specific humidity variability is mainly located in the tropics where moisture is abundant and small- and meso-scale weather systems prevail. This is obviously different from the spatial distribution characteristics of "O−B" standard deviation.

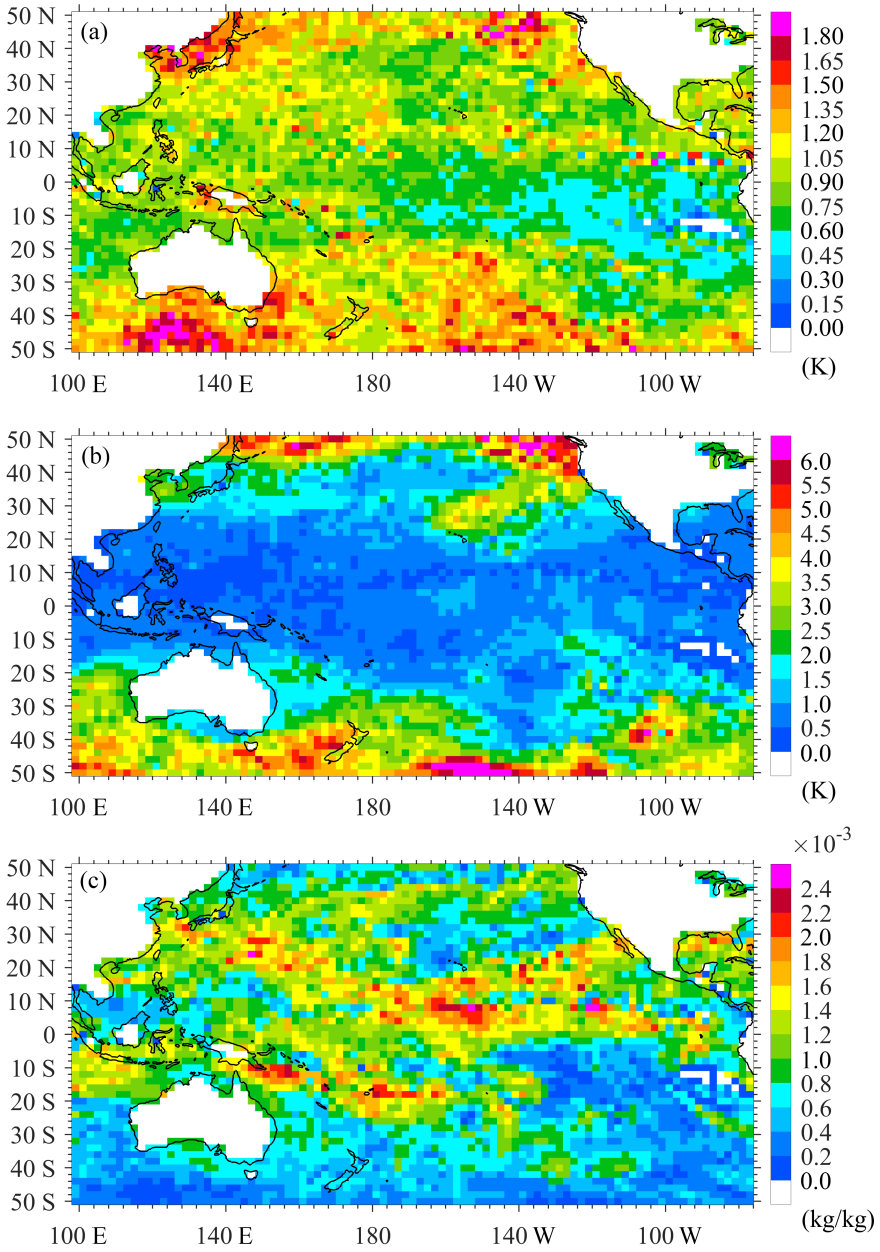

Figure 9. Spatial distribution of: (**a**) "O−B" standard deviation (unit: K) for Channel 13 (WF peaks at 600 hPa); (**b**) variability of atmospheric temperature (unit: K); and (**c**) specific humidity (unit: kg/kg) at 600 hPa of ERA-5 from 24 September to 8 October 2021. The blank boxes in the Eastern Pacific are caused by quality control.

Channel 6 is one of the 118-GHz channels, and its peak weighting function is at approximately 350 hPa. As can be seen from Figure 10a, the spatial variability of "O−B" standard deviation for Channel 6 is relatively small, basically between 0.4–0.6 K. There are no complex weather signals, and the large "O−B" standard deviation is mainly located in the tropical region. Obviously, the "O−B" standard deviation for Channel 6 has no significant correlation with temperature or specific humidity variability at 350 hPa. For example, in the low water vapor variability area in the eastern tropical Pacific, the standard deviation of "O−B" is approximately 0.5 K, as in the surrounding area.

The other channels also show similar results, and these results also fully demonstrate the suitability of background field for MWHS-2 data evaluation.

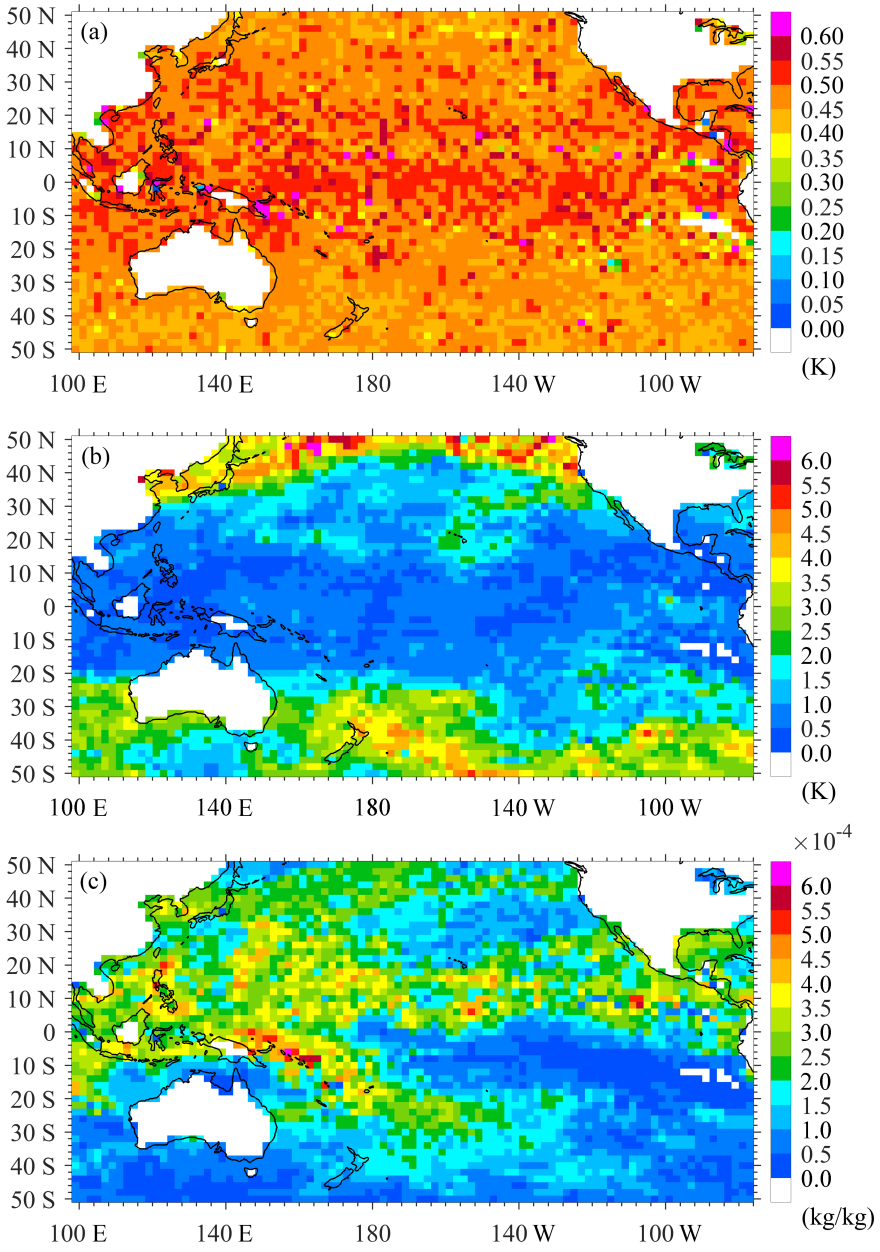

Figure 10. Spatial distribution of: (**a**) "O−B" standard deviation (unit: K) for Channel 6 (WF peaks at 350 hPa); (**b**) variability of atmospheric temperature (unit: K); and (**c**) specific humidity (unit: kg/kg) at 350 hPa of ERA-5 from 24 September to 8 October 2021. The blank boxes in the Eastern Pacific are caused by quality control.

5. Observation Noises

As mentioned above, FY-3E MWHS-2 has noises in both the along-track direction and the along-scan direction, namely, the striping noise and the high-frequency oscillation noise (hereafter mentioned as the along-scan noise). Additionally, the observation noise will have adverse effects on data application, such as increasing the inter-channel correlations between the channels in data assimilation [34,35]; thus, noise filtering is very significant.

Striping noise is common in the new generation of high-resolution microwave sounders onboard polar orbiting satellites. Although the cause of striping noise generation is still controversial, many mitigation methods have been developed by our predecessors [34,36,37]. To clarify the characteristics of striping noise, this study adopts the method developed by Qin et al. [34] to extract the striping noise of the instrument. The main principle of this method is to decompose the observed brightness temperature using the Principal Component Analysis method and then to smooth the PC coefficient. The striping noise is mainly contained in the first three PC modes according to its characteristic of fixing along the scanning direction. Meanwhile, according to the randomness of the weather systems, the first three modes mainly represent the "climate state" of the bright temperature with gentle spatial variation. In general, the striping noise can be removed without losing the weather signal by filtering the small-scale disturbance from the first PC coefficient and then combining it with the first mode to reconstruct the brightness temperature. Due to the randomness of the striping noise, the Ensemble Empirical Mode Decomposition (EEMD) [38] is employed to smooth the PC coefficients. Since the EEMD method can be used to decompose a signal based on the scale characteristics of itself without setting basis functions with fixed frequency beforehand, this method is ideal for filtering striping noise with no fixed frequency. Detailed discussions of the EEMD methods can be found in Wu et al. [38].

Figure 11a,b show the striping noise isolated from the observations in Figure 2a and the new "O−B" distribution after the striping noise mitigation. The striping noise for Channel 3 is at approximately 0.2 K with a relatively uniform global distribution, indicating that noise extraction is not affected by the original brightness temperature distribution. Compared with Figure 2c, the striping noise in the "O−B" distribution in Figure 11b is significantly weakened, while the other features are successfully retained.

According to Figure 6a,b, obvious jitters with scanning angles are found in MWHS-II, which is also found in the microwave humidity sounders carried by the early Fengyun series satellites. Thus, Zou et al. [35,39] and Zhu et al. (2021) developed a noise filtering method to compare the characteristics of the along-scan noises in different Fengyun series microwave humidity sounders and found that the along-scan noise is significantly weakened with the instrument upgrade. The method proposed by Zou et al. [39] was also used to extract the along-scan noise to further clarify its influence. Zou et al. [39] found that the along-scan noise has a similar characteristic to the striping noise; in addition, the striping noise is relatively fixed along the scanline, while the along-scan noise is relatively fixed along the track. Therefore, by decomposing the brightness temperature and simply applying the five-point smoothing to the first mode from Principal Component Analysis, the along-scan noises can be well removed from the observations. Figure 12 shows the noise distribution after subtracting the reconstructed brightness temperature from the observation for the 600 scanlines in Channel 3. The noise value is approximately 0.3 K, and the noise of the second and 97th FOV is significantly larger, which may result from the large errors of the two-edge FOVs (i.e., the first and 98th FOV).

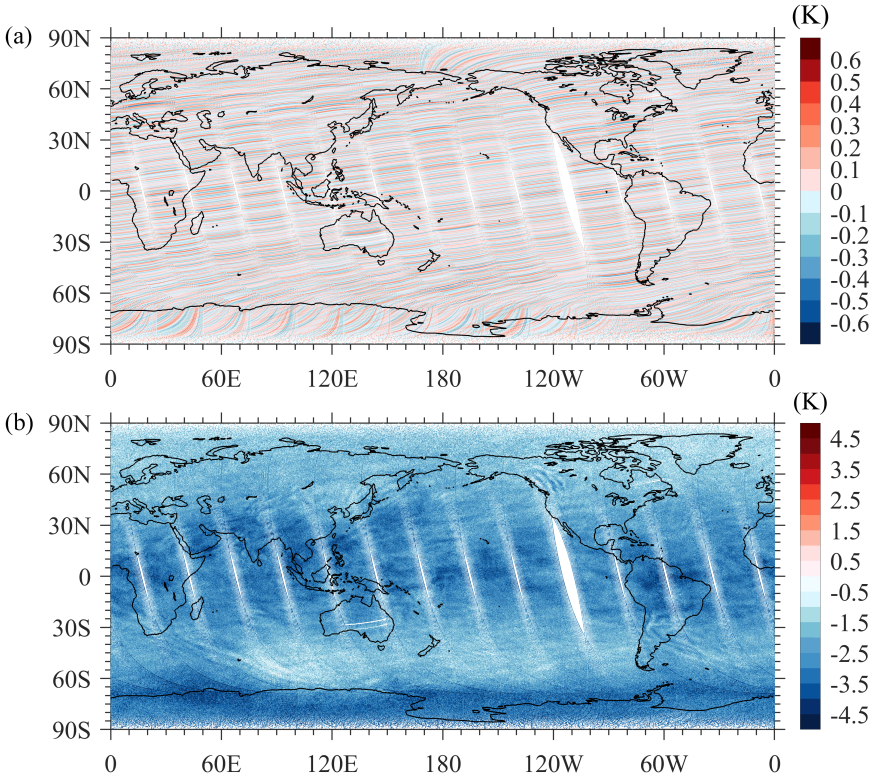

Figure 11. Spatial distribution of the: (**a**) striping noise (unit: K); and (**b**) "O−B" (unit: K) after the striping noise mitigation for MWHS-2 Channel 3 on 2 October 2021.

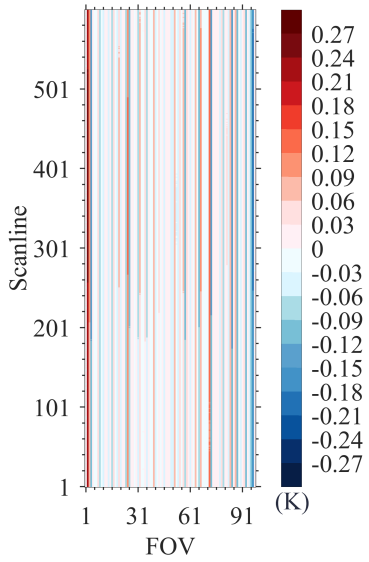

Figure 12. The along-scanline noises (unit: K) of 600 scanlines for Channel 3.

The biases of each channel after noise mitigation are shown in Figure 13. Originally, the biases for all the channels have high-frequency oscillations along the scanlines, with basically the same oscillation directions. After the brightness temperature reconstruction, the overall trend of the biases with FOVs does not change, but the high-frequency oscillations are eliminated to some extent, indicating that the along-scan noises are suppressed well.

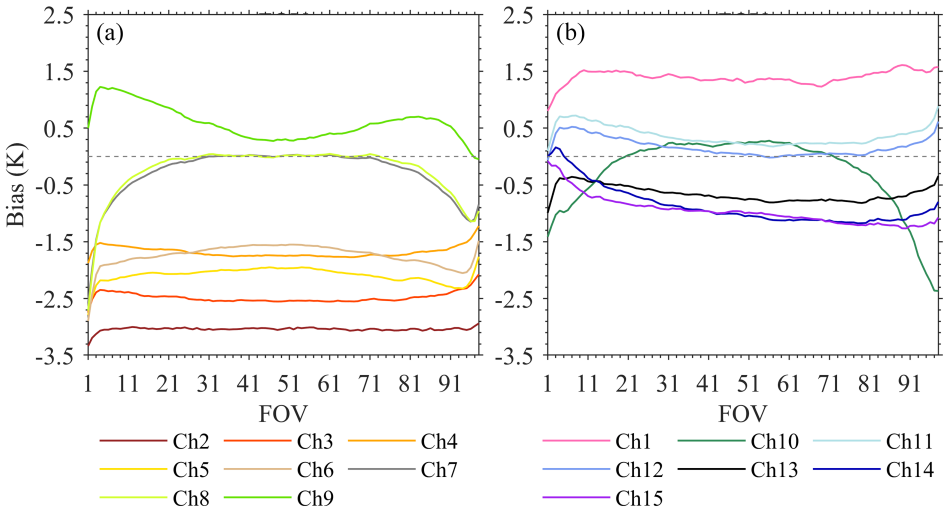

Figure 13. Observation biases (unit: K) varying with the FOVs for (**a**) the 118-GHz channels and (**b**) the other channels after removing the along-scan noises.

Figure 14 shows the "O−B" standard deviations after noise filtering. Different from the bias changes, the standard deviations are only slightly smoothed in individual channels, with values almost remaining unchanged, further proving that the noise filtering method has little impact on the other signals in addition to the along-scan noise; thus, the error characteristic basically survives.

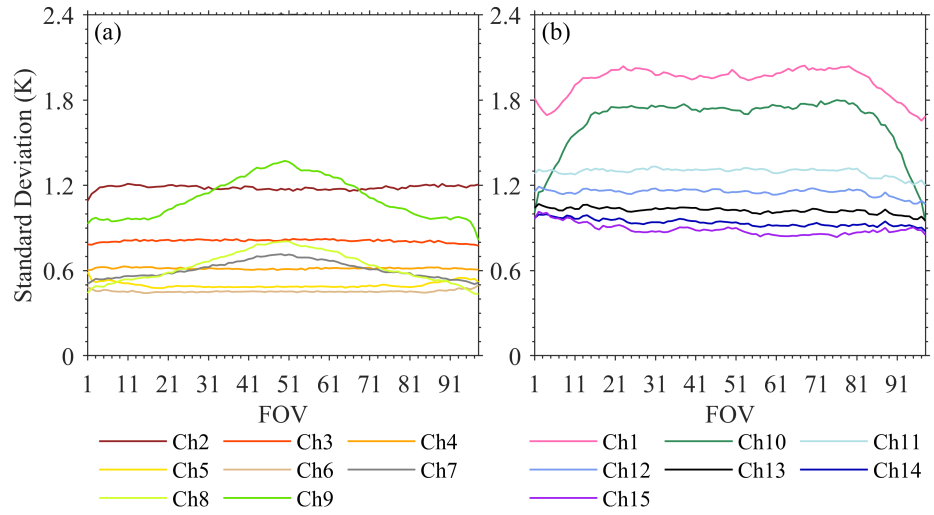

Figure 14. The standard deviations of "O−B" (unit: K) varying with the FOVs for (**a**) the 118-GHz channels and (**b**) the other channels after removing the along-scan noises.

6. Conclusions

Detailed assessment of the bias and error characteristics is a prerequisite for effective satellite data assimilation. Data from the fifteen days of the Pacific Ocean clear-sky observations between 50°S and 50°N were used to quantitatively evaluate the bias and error characteristics of MWHS-2 onboard FY-3E, a newly launched satellite in the early-morning orbit. In general, the biases of all the channels were within a reasonable range of −4 K to 2 K, most of which were negative. The standard deviations of all the channels were less than 2 K, most of which were within 1.5 K except for the two window channels. As a cross-track scanning instrument, the bias and standard deviation of the "O−B" for MWHS-2 varied with the scanning angles and latitude bands. The biases for water vapor detection channels were nonsymmetrical about the FOVs, which may be caused by antenna pointing error or polarization misalignment. The standard deviations of the window channels and low-level

sounding channels near 118.75 GHz increased with decreasing scanning angles, while the standard deviations of the other channels were relatively stable along the scanlines. The linear variation in the bias with the latitude is significant in the window channels, water vapor absorption channels and 118-GHz high-level sounding channels. The standard deviation increased with the latitude in the window channels, water vapor detection channels, and Channels 2 and 9. Such variations with latitude bands are obviously stronger than the microwave temperature sounder carried with the same satellite, which also indicates that special attention should be given to the bias correction and observation error setting with latitude bands in the application of MWHS-2 data assimilation.

During the analysis of the bias characteristics, both striping noise and along-scan noise were found in FY-3E MWHS-2. To clarify the magnitude of the noises in the instrument, noise filtering methods developed by our predecessors were introduced in this study to extract the two kinds of noises. The results show that the noise filtering method can mitigate the observation noise well without losing the original weather signals. The striping noises and the along-scan noises are all approximately 0.2 K, which is much smaller than the noise equivalent temperature difference of the instrument.

Due to the limitation of the data quantity, the results in this study are still uncertain, especially without considering the variation characteristics of the biases and errors with time (such as daytime or seasonal), geographical location, weather system and underlying surface (such as land, sea or ice) [19], which are the targets of subsequent research.

Author Contributions: Conceptualization, J.M. and Z.Q.; methodology, J.M.; software, J.M.; validation, Z.Q., J.L. and J.H.; formal analysis, J.M. and Z.Q.; investigation, J.M. and Z.Q.; resources, J.L. and Y.H.; data curation, J.L. and J.H.; writing—original draft preparation, J.M.; writing—review and editing, J.M., Z.Q. and Y.H.; visualization, J.M.; supervision, Z.Q., J.L. and J.H.; project administration, Z.Q.; funding acquisition, Z.Q. All authors have read and agreed to the published version of the manuscript.

Funding: This research was jointly funded by the National Key R&D Program of China (Grant 2018YFC1507302), the Youth Project of the National Natural Science Foundation of China (41805076), the Natural Science Foundation of Jiangsu Province (BK20211396) and the Fengyun Application Pioneering Project (FY-APP-2021.0201).

Data Availability Statement: The data used for RTM simulations are available at https://cds.climate.copernicus.eu/cdsapp#!/dataset/reanalysis-era5-pressure-levels-preliminary-back-extension?tab=form, https://cds.climate.copernicus.eu/cdsapp#!/dataset/reanalysis-era5-single-levels-preliminary-back-extension?tab=form (accessed on 26 July 2022).

Acknowledgments: The authors would like to thank the National Satellite Meteorological Center of Chinese Meteorology Administration for the FY-3E MWHS-2 data (https://pan.baidu.com/disk/main?from=homeFlow#/index?category=all&path=%2F%E5%8D%AB%E6%98%9F (accessed on 26 July 2022)) and the RTTOV coefficients. All data used in this paper are available from the authors upon request (jaly@nuist.edu.cn).

Conflicts of Interest: The authors declare no conflict of interest.

Abbreviations

The following abbreviations are used in this manuscript:

AMSR-E	Advanced Microwave Scanning Radiometer for EOS
ECMWF	European Centre for Medium-Range Weather Forecasting
EEMD	Ensemble Empirical Mode Decomposition
ERA-5	ECMWF 5th-Generation Reanalysis
FOV	field of view
FY-3E	Fengyun-3E
MWTS	MicroWave Temperature Sounder
MWHS	MicroWave Humidity Sounder
NCEP	National Centers for Environmental Prediction

NOAA	National Oceanic and Atmospheric Administration
NWP	numerical weather prediction
QH	quasi-horizontal
QV	quasi-vertical
RTTOV	Radiative Transfer for TIROS Operational Vertical Sounder
RTM	radiative transfer model
WF	weighting function

References

1. Zhang, P.; Hu, X.; Lu, Q.; Zhu, A.; Lin, M.; Sun, L.; Chen, L.; Xu, N. FY-3E: The first operational meteorological satellite mission in an early-morning orbit. *Adv. Atmos. Sci.* **2021**, *39*, 1–8. [CrossRef]
2. Guerbette, J.; Mahfouf, J.F.; Plu, M. Towards the assimilation of all-sky microwave radiances from the SAPHIR humidity sounder in a limited area NWP model over tropical regions. *Tellus A Dyn. Meteorol. Oceanogr.* **2016**, *68*, 28620. [CrossRef]
3. Candy, B.; Migliorini, S. The assimilation of microwave humidity sounder observations in all-sky conditions. *Q. J. R. Meteorol. Soc.* **2021**, *147*, 3049–3066. [CrossRef]
4. Li, J.; Zhang, S.; Jiang, J.; Dong, X. In-orbit performance of Microwave Humidity Sounder (MWHS) of the Chinese FY-3 meteorological satellite. In Proceedings of the 2010 IEEE International Geoscience and Remote Sensing Symposium, Honolulu, HI, USA, 25–30 July 2010; IEEE: Piscataway, NJ, USA, 2010; pp. 574–577.
5. Zou, X.; Wang, X.; Weng, F.; Li, G. Assessments of Chinese Fengyun Microwave Temperature Sounder (MWTS) measurements for weather and climate applications. *J. Atmos. Ocean. Technol.* **2011**, *28*, 1206–1227. [CrossRef]
6. Dee, D.P. Bias and data assimilation. *Q. J. R. Meteorol. Soc.* **2005**, *131*, 3323–3343. [CrossRef]
7. Benáček, P.; Mile, M. Satellite bias correction in the regional model ALADIN/CZ: Comparison of different varBC approaches. *Mon. Weather Rev.* **2019**, *147*, 3223–3239. [CrossRef]
8. Collard, A.; McNally, A. The assimilation of infrared atmospheric sounding interferometer radiances at ECMWF. *Q. J. R. Meteorol. Soc.* **2009**, *135*, 1044–1058. [CrossRef]
9. Guidard, V.; Fourrié, N.; Brousseau, P.; Rabier, F. Impact of IASI assimilation at global and convective scales and challenges for the assimilation of cloudy scenes. *Q. J. R. Meteorol. Soc.* **2011**, *137*, 1975–1987. [CrossRef]
10. Waller, J.A.; Ballard, S.P.; Dance, S.L.; Kelly, G.; Nichols, N.K.; Simonin, D. Diagnosing horizontal and inter-channel observation error correlations for SEVIRI observations using observation-minus-background and observation-minus-analysis statistics. *Remote Sens.* **2016**, *8*, 581. [CrossRef]
11. Chapnik, B.; Desroziers, G.; Rabier, F.; Talagrand, O. Diagnosis and tuning of observational error in a quasi-operational data assimilation setting. *Q. J. R. Meteorol. Soc.* **2006**, *132*, 543–565. [CrossRef]
12. Salonen, K.; Bormann, N. Accounting for the situation-dependence of the AMV observation error in the ECMWF system. In Proceedings of the 11th International Winds Workshop, Auckland, New Zealand, 13–15 November 2012.
13. Weston, P.; Bell, W.; Eyre, J. Accounting for correlated error in the assimilation of high-resolution sounder data. *Q. J. R. Meteorol. Soc.* **2014**, *140*, 2420–2429. [CrossRef]
14. Qin, Z.; Zou, X. Impact of AMSU-A data assimilation over high terrains on QPFs downstream of the Tibetan Plateau. *J. Meteorol. Soc. Jpn. Ser. II* **2019**, *97*, 1137–1154. [CrossRef]
15. Qin, Z. Adding CO_2 channel 16 to AHI data assimilation over land further improves short-range rainfall forecasts. *Tellus A Dyn. Meteorol. Oceanogr.* **2020**, *72*, 1–19. [CrossRef]
16. Harris, B.; Kelly, G. A satellite radiance-bias correction scheme for data assimilation. *Q. J. R. Meteorol. Soc.* **2001**, *127*, 1453–1468. [CrossRef]
17. Zhao, L.; Yang, Z.L.; Hoar, T.J. Global soil moisture estimation by assimilating AMSR-E brightness temperatures in a coupled CLM4–RTM–DART system. *J. Hydrometeorol.* **2016**, *17*, 2431–2454. [CrossRef]
18. Li, X.; Zou, X.; Zeng, M. An alternative bias correction scheme for CrIS data assimilation in a regional model. *Mon. Weather Rev.* **2019**, *147*, 809–839. [CrossRef]
19. Auligné, T.; McNally, A.; Dee, D. Adaptive bias correction for satellite data in a numerical weather prediction system. *Q. J. R. Meteorol. Soc.* **2007**, *133*, 631–642. [CrossRef]
20. Han, W.; Bormann, N. *Constrained Adaptive Bias Correction for Satellite Radiance Assimilation in the ECMWF 4D-Var System*; European Centre for Medium-Range Weather Forecasts: Reading, UK, 2016; pp. 1–31.
21. Lu, Q.; Bell, W.; Bauer, P.; Bormann, N.; Peubey, C. Characterizing the FY-3A microwave temperature sounder using the ECMWF model. *J. Atmos. Ocean Technol.* **2011**, *28*, 1373–1389. [CrossRef]
22. Guan, L.; Zou, X.; Weng, F.; Li, G. Assessments of FY-3A microwave humidity sounder measurements using NOAA-18 microwave humidity sounder. *J. Geophys. Res. Atmos.* **2011**, *116*. [CrossRef]
23. Wang, X.; Zou, X. Quality assessments of Chinese FengYun-3B microwave temperature sounder (MWTS) measurements. *IEEE Trans. Geosci. Remote Sens.* **2012**, *50*, 4875–4884. [CrossRef]
24. Han, Y.; Hou, X. Evaluation of the in-orbit performance of the microwave temperature sounder onboard the FY-3D satellite using different radiative transfer models. *J. Quant. Spectrosc. Radiat. Transf.* **2020**, *253*, 107041. [CrossRef]

25. Hersbach, H.; Bell, B.; Berrisford, P.; Hirahara, S.; Horányi, A.; Muñoz-Sabater, J.; Nicolas, J.; Peubey, C.; Radu, R.; Schepers, D.; et al. The ERA5 global reanalysis. *Q. J. R. Meteorol. Soc.* **2020**, *146*, 1999–2049. [CrossRef]
26. Ali, A.D.; Rosenkranz, P.W.; Staelin, D.H. Atmospheric sounding near 118 GHz. *J. Appl. Meteorol. Climatol.* **1980**, *19*, 1234–1238. [CrossRef]
27. Gu, S.; Guo, Y.; Wang, Z.; Lu, N. Calibration analyses for sounding channels of MWHS onboard FY-3A. *IEEE Trans. Geosci. Remote Sens.* **2012**, *50*, 4885–4891. [CrossRef]
28. Guo, Y. Introduction to FY-3E/MWHS-2 Instrument and Its L1 Product. Available online: http://img.nsmc.org.cn/PORTAL/NSMC/VIDEO/FY3E/20220107/07_MWHS.PDF (accessed on 7 January 2022).
29. Saunders, R.; Hocking, J.; Turner, E.; Rayer, P.; Rundle, D.; Brunel, P.; Vidot, J.; Roquet, P.; Matricardi, M.; Geer, A.; et al. An update on the RTTOV fast radiative transfer model (currently at version 12). *Geosci. Model Dev.* **2018**, *11*, 2717–2737. [CrossRef]
30. Andrey-Andrés, J.; Fourrié, N.; Guidard, V.; Armante, R.; Brunel, P.; Crevoisier, C.; Tournier, B. A simulated observation database to assess the impact of the IASI-NG hyperspectral infrared sounder. *Atmos. Meas. Tech.* **2018**, *11*, 803–818. [CrossRef]
31. Zou, X.; Zhuge, X.; Weng, F. Characterization of bias of Advanced Himawari Imager infrared observations from NWP background simulations using CRTM and RTTOV. *J. Atmos. Ocean Technol.* **2016**, *33*, 2553–2567. [CrossRef]
32. Andersson, E.; Haseler, J.; Undén, P.; Courtier, P.; Kelly, G.; Vasiljevic, D.; Brankovic, C.; Gaffard, C.; Hollingsworth, A.; Jakob, C.; et al. The ECMWF implementation of three-dimensional variational assimilation (3D-Var). III: Experimental results. *Q. J. R. Meteorol. Soc.* **1998**, *124*, 1831–1860. [CrossRef]
33. Weng, F.; Zhao, L.; Ferraro, R.R.; Poe, G.; Li, X.; Grody, N.C. Advanced microwave sounding unit cloud and precipitation algorithms. *Radio Sci.* **2003**, *38*, 33-1–33-13 [CrossRef]
34. Qin, Z.; Zou, X.; Weng, F. Analysis of ATMS striping noise from its Earth scene observations. *J. Geophys. Res. Atmos.* **2013**, *118*, 13–214. [CrossRef]
35. Zhu, L.; Qin, Z.; Min, J.; Xue, M. Characterizing, Mitigating, and Comparing the Along-Scanline Noise in Fengyun-3 Series Microwave Humidity Sounders (MWHSs). *IEEE Trans. Geosci. Remote Sens.* **2021**, *60*, 1–10. [CrossRef]
36. Ma, Y.; Zou, X. Striping noise mitigation in ATMS brightness temperatures and its impact on cloud LWP retrievals. *J. Geophys. Res. Atmos.* **2015**, *120*, 6634–6653. [CrossRef]
37. Zou, X.; Dong, H.; Qin, Z. Striping noise reduction for ATMS window channels using a modified destriping algorithm. *Q. J. R. Meteorol. Soc.* **2017**, *143*, 2567–2577. [CrossRef]
38. Wu, Z.; Huang, N.E. Ensemble empirical mode decomposition: A noise-assisted data analysis method. *Adv. Adapt. Data Anal.* **2009**, *1*, 1–41. [CrossRef]
39. Zou, X.; Ma, Y.; Qin, Z. Fengyun-3B microwave humidity sounder (MWHS) data noise characterization and filtering using principle component analysis. *IEEE Trans. Geosci. Remote Sens.* **2012**, *50*, 4892–4902. [CrossRef]